Electronic Supplementary Material (ESI) for Chemical Science. This journal is © The Royal Society of Chemistry 2021

Electronic supporting information

Inorganic cation-tailored “trapdoor” effect of the silicoaluminophosphate zeolite for highly selective CO_2 separation

Xiaohe Wang,[a]+ Nana Yan,[b]+ Miao Xie,[c]+ Puxu Liu, [d] Pu Bai,[a] Haopeng Su,[a] Binyu Wang,[a] Yunzheng Wang,[a] Libo Li,[d] Tao Cheng,[c] Peng Guo*[b], Wenfu Yan,*[a] Jihong Yu*[a,e]

[a] State Key Laboratory of Inorganic Synthesis and Preparative Chemistry, College of Chemistry, Jilin University, Changchun 130012 (P. R. China)

[b] National Engineering Laboratory for Methanol to Olefins, Dalian National Laboratory for Clean Energy, Dalian Institute of Chemical Physics, Chinese Academy of Sciences, Dalian 116023, China

[c] Institute of Functional Nano & Soft Materials (FUNSOM) and Jiangsu Key Laboratory for Carbon-Based Functional Materials & Devices, Soochow University, Suzhou 215123, China

[d] National Engineering Laboratory for Methanol to Olefins, Dalian National Laboratory for Clean Energy, Dalian Institute of Chemical Physics, Chinese Academy of Sciences, Dalian 116023, China

[e] International Center of Future Science, Jilin University, Changchun 130012, China

* Co-corresponding authors
Email: yanw@jlu.edu.cn, jihong@jlu.edu.cn, pguo@dicp.ac.cn

Table of contents in Supporting Information:

Section 1. Experimental details for the synthesis and ion-exchange of SAPO-RHOs S4

Section 2. Characterizations S4

Section 3. Detailed description on the crystallographic analysis of SAPO-RHO and M-SAPO-RHO after dehydration S5

Section 4. Detailed description on the measurements of CO_2, N_2, and CH_4 isotherms S5

Section 5. Separation factor (α) S5

Section 6. Detailed simulation method and model S5

Section 7. Breakthrough experiments S7

Section 8. Separation factor calculated from the breakthrough experiment S8

Fig. S1. Simulated PXRD pattern of SAPO-RHO and experimental ones of the as-synthesized SAPO-RHO and ion exchanged M-SAPO-RHOs (M = Na, K, and Cs) S9

Fig. S2. SEM images of as-synthesized SAPO-RHO and ion-exchanged M-SAPO-RHO (M = Na, K, and Cs) S9

Fig. S3. EDS mapping of (a) SAPO-RHO, (b) Na-SAPO-RHO, (c) K-SAPO-RHO, and (d) Cs-SAPO-RHO S10

Fig. S4. CO_2 (solid), CH_4 (semi solid) and N_2 (hollow) adsorption isotherms for (a) H- SAPO-RHO, (b) Na-SAPO-RHO, (c) K-SAPO-RHO, and (d) Cs-SAPO-RHO at 273 K (black), 298 K (red), 313 K (blue) S10

Fig. S5. Rate of adsorption curves for H-SAPO-RHO, Na-SAPO-RHO, K-SAPO-RHO, and Cs-SAPO-RHO of CO_2 at 298K and 1.0bar S11

Fig. S6. N_2 adsorption/desorption isotherms of the three batches of Na-SAPO-RHO at 77 K S11

Fig. S7. The pure component adsorption isotherms of the three different batches of Na-SAPO-RHO for CO_2 (a), CH_4 (b), and N_2 (c) and the average uptake of CO_2 (d), CH_4 (e), and N_2 (f) with error bars S12

Fig. S8. The separation factors of the three batches of Na-SAPO-RHO for CO_2/CH_4 (a) and CO_2/N_2 (b) S12

Fig. S9. The optimized adsorption structures of (a) CO_2, (b) CH_4, and (c) N_2 on Na-SAPO-RHO predicted from DFT calculations S13

Fig. S10. The isosteric heat of adsorption (Q_{st}) of CO_2 for Na-SAPO-RHO S13

Fig. S11. The optimized adsorption structures of (a) CO_2, (b) CH_4, and (c) N_2 on K-SAPO-RHO and (d) CO_2, (e) CH_4, and (f) N_2 on Cs-SAPO-RHO predicted from DFT calculations S14

Fig. S12. Simulated PXRD pattern of SAPO-RHO and experimental ones of the calcined Na-SAPO-RHO S14

Fig. S13. N_2 adsorption/desorption isotherms of the calcined SAPO-RHO and Na-SAPO-RHOs at 77 K S15

Fig. S14. Comparison of the CO_2 (a), CH_4 (b), and N_2 (c) adsorption isotherms of all Na-SAPO-RHOs at 298 K between 0-1 bar, Comparison of the CO_2 uptake for all Na-SAPO-RHOs under 0.02 and 0.15 bar, respectively at 298 K(d), CO_2/CH_4 separation factors at 0.02/0.98 bar (e), and CO_2/N_2 separation factors at 0.15/0.85 bar (f) at 298 K for all Na-SAPO-RHOs S15

Fig. S15. CO_2/CH_4 (left) and CO_2/N_2 (right) breakthrough curves on Na-SAPO-RHO using CO_2/CH_4 (50:50, v/v) and CO_2/N_2 (15:85, v/v) gas mixtures with a total gas flow rate of 5 mL/min at 298 K, respectively S16

Fig. S16. The breakthrough value estimated from the breakthrough curves for CO_2/CH_4 mixture S16

Fig. S17. The dynamic separation factors of the batch 1 of Na-SAPO-RHO for CO_2/CH_4 and CO_2/N_2 S16

Table S1. The composition and textual properties of H-SAPO-RHO and calcined M-SAPO-RHO (M = Na, K, and Cs) S17
Table S2. Space groups of aluminosilicate zeolite Rho and SAPO-RHO S17
Table S3. Crystallographic details of Rietveld refinements of M-SAPO-RHO samples S17
Table S4. Unit cell composition, space group, minimum O-O distance of 8MR windows, minimum M-O distance and cation site occupancies in dehydrated SAPO-RHO (Site I, *d*8*r*; Site II, *s*8*r*; Site III, *s*6*r*) and total M atom in the unit cell S18
Table S5. The textual properties of the three batches of Na-SAPO-RHO S18
Table S6. Calculated adsorption enthalpy H_{ads} (eV) of CO_2, N_2 and CH_4 molecule in Na-SAPO-RHO, K-SAPO-RHO, and Cs-SAPO-RHO system S18
Table S7. The saturated adsorption amount of CO_2, CH_4, and N_2 of the batch 1 of Na-SAPO-RHO for CO_2/CH_4 and CO_2/N_2 S19
References S19

Section1. Synthesis and ion-exchange

Chemical and materials: Ludox AS-40 (Aldrich; 40 wt%, suspension in water), Pseudo-boehmite (Sasol, 72.7 wt%), Phosphoric acid (Beijing Chemical Reagent Factory, 85 wt%), Cetyltrimethylammonium bromide (Sinopharm Chemical Reagent Co.,Ltd), LiCl ,NaCl, KCl (Tianjin Fuchen Chemical Reagent Factory), CsCl (Aladdin ®), Diaethylamin (99.0%), Deionized water. All reagents were used without purification.

Synthesis：The SAPO-RHO was synthesized by the seed-assisted method using DEA as a template with the molar composition of 2.4 DEA: 1.0 Al_2O_3: 1.0P_2O_5: 0.6SiO_2: 0.03 CTAB: 40H_2O: 10% seed (10 wt% of SiO_2) under hydrothermal conditions at 473 K for 48 h. A homogenous solution was prepared by dissolving 4.2 g pseudo-boehmite (72.7wt%) in mixture of 6.9 g orthophosphoric acid (85.0%) and 7 g deionized water, followed by a continuous stirring at room temperature for 2 h. Then, 2.7 g AS-40 (40%) added into the above mixture. After a continuous stirring for 30 min, 1.0 g cetyltrimethylammonium bromide (CTAB) was added into the mixture and continuous stirring for 30 min with the final addition of 5.25 g DEA template and further stirred for 2 h to obtain a homogeneous gel. Finally, the seeds were added into the solution and then stirred until the seed dissolved completely. The crystallization was carried out in a stainless-steel autoclave at 473 K for 48 h. The product was filtered, washed three times with ethanol and three times with deionized water and dried at 373 K overnight and calcined at 873 K for 4h to remove the organic species for further characterizations.

Ion-exchange：The as-synthesized SAPO-RHO was added into the solution containing target ions (Na^+, K^+, and Cs^+) with the solid (g): liquid (mL)= 1:50 (0.5 mol/L MCl solution) and stirred at 333 K for 4 h for three times. Afterwards, the solid was separated, washed, dried at 373 K and calcined at 873 K for 4 h to remove the organic species for further characterizations.

Section 2. Characterizations.

Powder X-ray diffraction (PXRD) analyses were performed by Rigaku D/Max 2550 X-ray diffractometer in the scanning range of 2θ between 4° and 40° with 6°/min using copper Kα as the source of radiation (λ=1.5418 Å). PXRD data used for Rietveld refinement was collected on the STOE STADI PESSENTIAL X-ray diffractometer equipped with a Mythen II detector in the Debye-Scherrer mode with Cu Kα1 radiation (λ=1.5406 Å) in the Debye-Scherrer mode. The morphology and microstructure were obtained with field emission scanning electron microscopy (SEM, JSM-7800F). The elemental mapping images were taken on Energy Dispersive Spectrometer (EDS) on Oxford X-MAX 80. N_2 adsorption/desorption measurements were carried out on a Micromeritics 2020 analyzer at 77 K. Prior to measurement, the samples were degassed at 623 K for at least 10 h. The textural properties including total surface area, external surface area, and micropore volume were measured using Brunauer-Emmett-Teller (BET) equation and t-plot method, respectively. The total pore volume was obtained from the capacity of N_2 adsorbed at P/P_0 = 0.99.

Section 3. Detailed description on the crystallographic analysis of SAPO-RHO and M-SAPO-

RHO after dehydration.

For Rietveld refinement, PXRD data of high resolution was collected on a STOE STADI P ESSENTIAL X-ray diffractometer equipped with a Mythen II detector with Cu Kα1 radiation (λ=1.5406 Å) in the Debye-Scherrer mode. Before collection, alkaline metal exchanged M-SAPO-RHO samples were transferred into a capillary with diameter of 0.2 mm and then dehydrated at 573 K for 12 h. After that, the capillary was sealed with wax and measured with 2θ angle range of 5-120°, step size of 0.015° and total counting time of 24 h at room temperature. The control sample, hydrated Cs-SAPO-RHO, was measured without dehydration. CCDC 2056931, 2056929, 2056930, 2056932 contain the supplementary crystallographic data for this paper. These data can be obtained free of charge from The Cambridge Crystallographic Data Centre (https://www.ccdc.cam.ac.uk).

Section 4. Detailed description on the measurement of CO_2, N_2, and CH_4 isotherms.

Single component equilibrium adsorption isotherms for N_2, CH_4, and CO_2 were performed on Micrometrics ASAP2020 instrument. Before each measurement, all the samples were degassed at 623K for 10 h under vacuum ($P/P_0=10^{-5}$) to desorb all adsorbed gases and water. Adsorption isotherms were then acquired at 273, 298, 313K and the temperatures were controlled by condensation pump and Dewar flask with the fluctuations less than ±0.2 K during the experiment.

Section 5. Separation factor (α).

Using the pure component isotherms, the adsorption selectivity is given as:

$$Selectivity = \frac{q_1/q_2}{p_1/p_2} \# \quad (1)$$

Where $q_{1,2}$ and $p_{1,2}$ are the uptake and the partial pressure of components 1 and 2, respectively.

Section 6. Detailed simulation method and model.

In order to further understand gas separation performance influenced by the locations of inorganic cations, we carried out the periodic DFT calculations using Vienna *ab initio* simulation package (VASP 5.4.4). The initial structural model of Na-SAPO-RHO with space group of *P*1 (including inorganic cations) was used from high symmetry one obtained from Rietveld refinement. Based on the unit cell compositions deduced from EDS, there are eight Na^+ ions per unit cell. Meanwhile, final Rietveld refinement result shows there are six Na^+ ions distributing in the single 8-rings (*s*8*r*) and two Na^+ ions locating in the single 6-rings (*s*6*r*) within one-unit cell. Eight P atoms per unit cell are replaced by eight Si atoms, which are close to Na^+ ions making the entire structure electroneutral. In this case, one reasonable Na-SAPO-RHO structural model is established for further calculation. We also utilized the same approach to build structural models of K/Cs-SAPO-RHO. Since there are only seven K^+ or Cs^+ in the K/Cs-SAPO-RHO unit cell, one more proton is introduced for making the entire structure electroneutral.

We carried out the density functional theory (DFT), and calculated the adsorption enthalpy of H_{ads} (eV) of CO_2, N_2, and CH_4 molecule in Na-SAPO-RHO, K-SAPO-RHO, and Cs-SAPO-RHO, and the results are given in Table S6. Optimized geometries of CO_2, CH_4, and N_2 adsorbed on Na-SAPO-RHO are shown in Fig. S9. For CO_2 adsorption, two Na^+ ions capture one CO_2 molecule: one is in the center of the *s6r* with the Na-O_{CO2} distance of 2.407 Å, while the other locates in the center of *s8r* with the Na-O_{CO2} distance of 2.713 Å. Such binding structures result from the facts that 1) O atom carries partial negative charges and 2) the size of CO_2 just matches the distance of two Na cations. It indicates a strong interaction of CO_2 to the Na-SAPO-RHO framework and DFT calculations predict an adsorption enthalpy (ΔH_{CO2}) of -42.58 kJ/mol, which is close to the experimental measurement of -38.9 kJ/mol (Fig. S10). According to these computational predictions, we conclude that Na-SAPO-RHO has a strong interaction with CO_2, which can well explain a higher CO_2 uptake at the low pressure.

Instead, the adsorption of CH_4 and N_2 in the Na-SAPO-RHO is weaker than that of CO_2 as indicated by the DFT calculations, which predict -30.12 kJ/mol enthalpy of CH_4 (ΔH_{CH4}) and -28.61 kJ/mol adsorption enthalpy of N_2 (ΔH_{N2}). The decrease adsorption is due to both the size and the hardness in polarization. The final DFT calculation results demonstrate that both CH_4 and N_2 interacts with the Na^+ in the *s6r* solely as shown in Fig. S9b and Fig. S9c.

Utilizing the same approach, we also conducted the calculations with K/Cs-SAPO-RHO. Final calculation results show that the most stable adsorption sites for CO_2, N_2, and CH_4 are the same, which interact with K/Cs^+ ions in *s6r* solely as shown in Fig. S11. However, such bindings are much weaker. For CO_2, ΔH_{CO2} decreases to -32.51 kJ/mol in K-SAPO-RHO, and further decreases to -29.52 kJ/mol in Cs-SAPO-RHO. Such decreases are mainly attributed to the fact that CO_2 only interacts with one inorganic cation, whose scenario is distinct from the structural feature observed in Na-SAPO-RHO, i.e., two inorganic cations capture one CO_2 molecule. The adsorption of CH_4 and N_2 also decreases after cation exchange. For CH_4, ΔH_{CH4} decreases to -20.66 kJ/mol in K-SAPO-RHO, and further decreases to -19.31 kJ/mol in Cs-SAPO-RHO. For N_2, ΔH_{N2} decreases to -20.31 kJ/mol in K-SAPO-RHO, and further decreases to -18.19 kJ/mol in Cs-SAPO-RHO. These DFT predictions are well consistent with the experimental observation.

All of the periodic DFT calculations were carried out using Vienna ab initio simulation package (VASP 5.4.4).[1] Moreover, the Perdew, Burke, and Ernzerhof (PBE) flavor[2] of density functional theory (DFT) with the post-stage DFT-D3 method was used to correct for London dispersion (van der Waals attraction) with Becke-Johnson damping.[3] The projector augmented wave (PAW) method [4] was used to account for core-valence interactions. The kinetic energy cutoff for plane wave expansions was set to 400 eV, and the Brillouin zones were sampled with the Monkhorst–Pack k-points of 1×1×1 for calculation. The convergence criteria were 1×10^{-5} eV energy differences for solving the electronic wave function. The Methfessel-Paxton smearing of second order with a width of 0.2 eV was applied. All atomic coordinates were converged to within 0.03 eV/Å for maximal components of forces.

The adsorption entropy is calculated as follows:

$$\Delta H_i = \Delta E_i + PV\#(2)$$

Here, *i* is the adsorption molecules (CO_2, CH_4 and N_2), *PV* is estimated basing on the approximation of ideal gas, and ΔE_i is the binding energy.

$$\Delta E_i = E_{i-SAPO-RHO} - (E_{i-SAPO-RHO} + \Delta E_i)\#(3)$$

Ten and eight Na^+ ions can be identified in the unit cell compositions of de-Na-SAPO-RHO and zeolite Na-Rho. Since there are two *lta* cages within one-unit cell, five and four ions are allocated in one *lta* cage of de-Na-

SAPO-RHO and zeolite Na-Rho on average. In this case, two neutral $Na_5Al_5Si_{43}O_{72}(OH)_{48}$ and $Na_4Si_4Al_{24}P_{20}O_{72}(OH)_{48}$ clusters cut from zeolite Na-Rho and de-Na-SAPO-RHO are utilized for the further theoretical calculations, in which the terminals of clusters are ended with OH groups.

All calculations were performed with the Gaussian 16 suite of programs (Revision A.01)[5]. The single-point energy of all cluster model of all model were calculated by density functional theory (DFT) calculations using the B3LYP functional[6] with 6-31G(d) basis set for all atoms. Meanwhile, to take the dispersion interactions into account, we consider the DFT-D3 dispersion correction.[3] The binding energy of Na^+ in the center of elliptical single 8-rings can be calculated using the following equation:

$$\Delta E = E_{Na^+} + E_{[Na_3Si_4Al_{24}P_{20}O_{72}(OH)_{48}]^-} - E_{Na_4Si_4Al_{24}P_{20}O_{72}(OH)_{48}} \#(4)$$

$$\Delta E = E_{Na^+} + E_{[Na_4Si_{43}Al_5O_{72}(OH)_{48}]^-} - E_{Na_5Si_{43}Al_5O_{72}(OH)_{48}} \#(5)$$

Section 7. Breakthrough experiments.

The breakthrough experiments for CO_2/CH_4 and CO_2/N_2 mixtures were carried out at a flow rate of 5 mL/min (298 K, 1.01 bar). Activated zeolites powder was packed into ϕ5.8×74.8 mm (valid column volume 2 cm^3, mass 1.3717 g) stainless steel column under pure N_2 atmosphere. The experimental set-up consisted of two fixed-bed stainless steel reactors. One reactor was loaded with the adsorbent, while the other reactor was used as a blank control group to stabilize the gas flow. The horizontal reactor loaded with adsorbent were placed in a temperature control environment, maintained at 298 K. The flow rates of all gases mixtures were regulated by mass flow controllers, and the effluent gas stream from the column was monitored by a gas chromatography (GC-2014C SHIMADZU, Al_2O_3 packed column, and TCD-Thermal Conductivity Detector, detection limit 0.01%). Prior to the breakthrough experiment, we firstly activated the sample at 623 K overnight at the activation station, then the dehydration sample was loaded and further activated in situ by flushing the adsorption bed with helium gas for 2 h at 523 K. After every separation operation, the adsorption bed was regenerated by purging with helium at a flow rate of 30 mL/min for 2 h at 298 K.

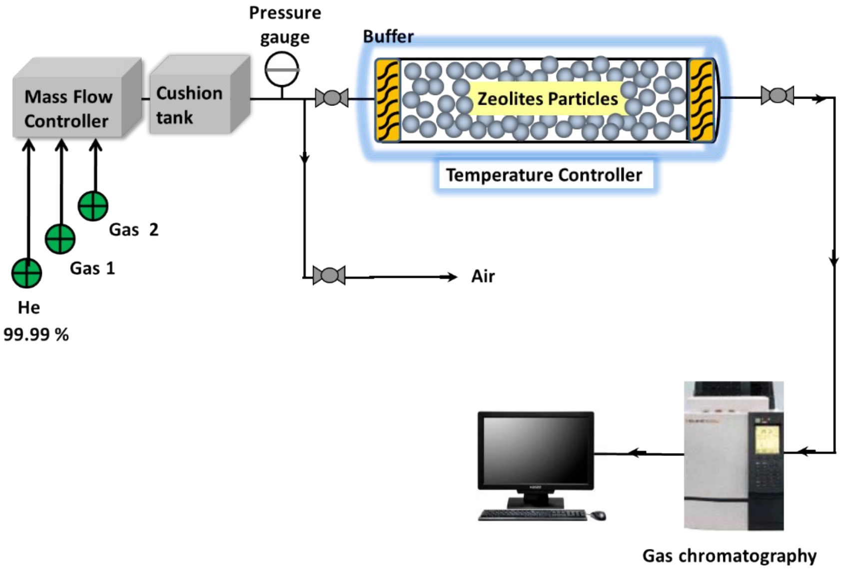

Schematic S1. The set up for the breakthrough experiments

Section 8. Separation factor calculated from the breakthrough experiment.

The equation used to estimate the selectivity from the breakthrough curves was identical to the separation factors describe in the section 5. To determine the adsorption amount at the mixed gas condition, the dynamic saturated adsorption capacity of each component ($q_{i,m}$) is calculated based on the breakthrough curves by the equation described as follows:

$$q_{i,m} = \frac{\int_{0}^{t_0} (F_i - F_e)\Delta t - V_{dead}}{m} \#(6)\#$$

where the F_i is the flow rate of specific gas at the inlet of the adsorption column with the unit of cm^3/min, while the F_e represents the effluent flow rate of the corresponding gas species; V_{dead} is the dead volume of the system (cm^3); m represents the mass of the adsorbent loaded into the adsorption column (g); t_0 is the retention time interval for the gas mixture. For example in **Fig. S16**, the CO_2 adsorption amount at dynamic condition was equal to the gray area, thus the $q_{co2}= Fe\times(S_{0\text{-}t2}\text{-}S_{t1\text{-}t2})/m=34.1\ cm^3/g$. While for the CH_4 adsorption, $q_{CH4}=Fe\times t_{(0\text{-}tbeak)}/m=0.0552\ cm^3/g$. The adsorption amount for CO_2 and N_2 at the mixed condition was also calculated with the same method.

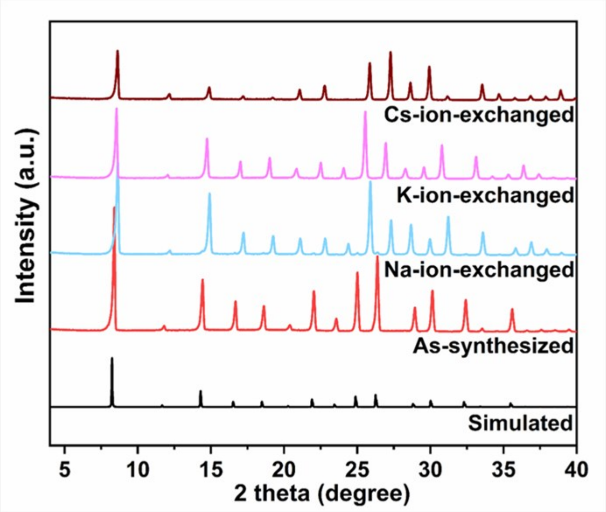

Fig. S1. Simulated PXRD pattern of SAPO-RHO and experimental ones of the as-synthesized SAPO-RHO and ion-exchanged M-SAPO-RHOs (M = Na, K, and Cs).

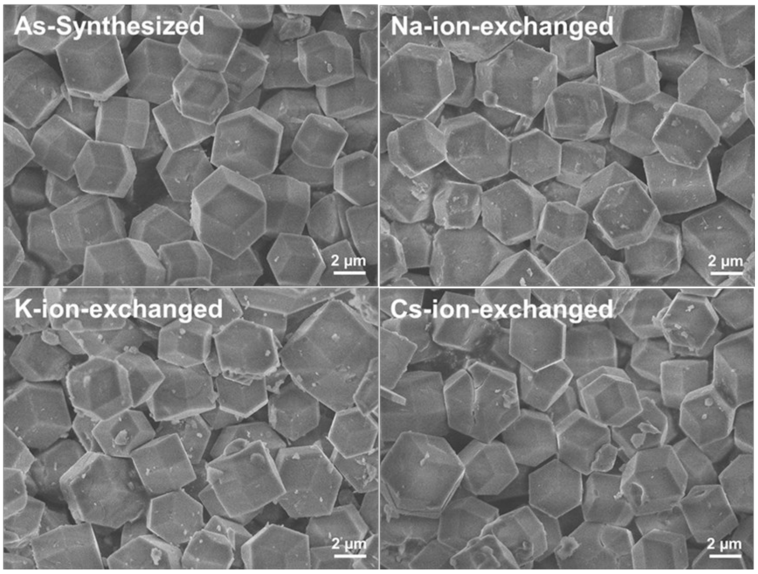

Fig. S2. SEM images of as-synthesized SAPO-RHO and ion-exchanged M-SAPO-RHO (M = Na, K, and Cs).

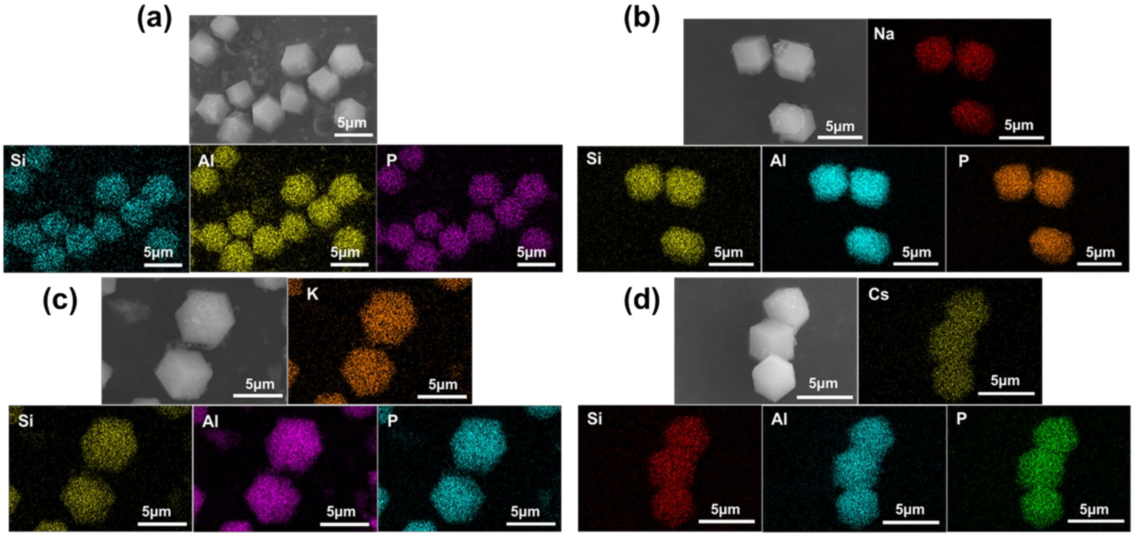

Fig. S3. EDS mapping of (a) SAPO-RHO, (b) Na-SAPO-RHO, (c) K-SAPO-RHO and (d) Cs-SAPO-RHO.

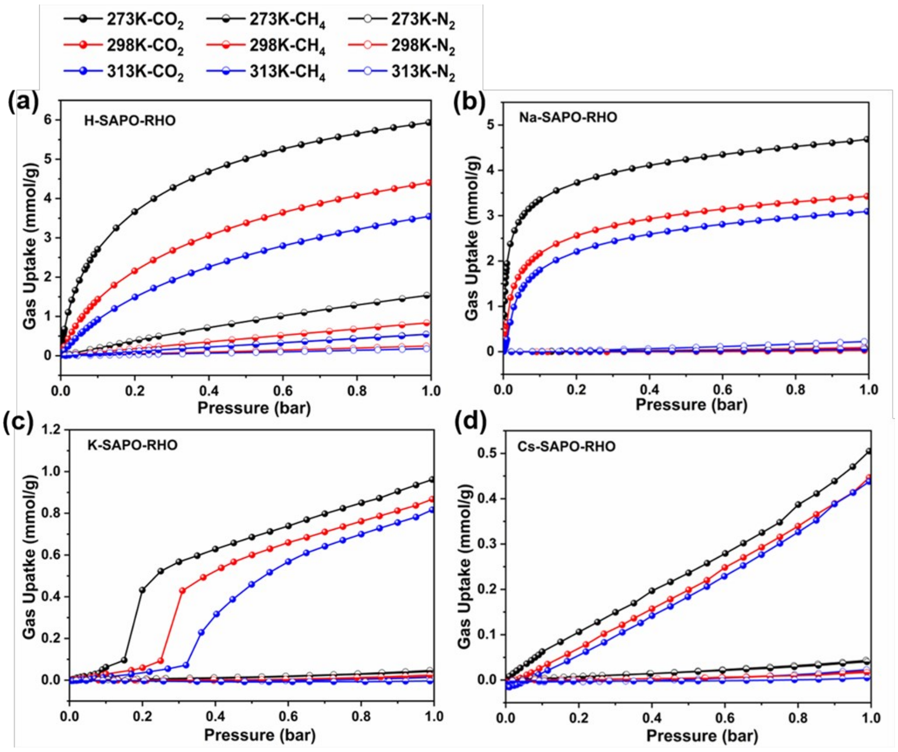

Fig. S4. CO_2 (solid), CH_4 (semi solid) and N_2 (hollow) adsorption isotherms for (a) H- SAPO-RHO, (b) Na-SAPO-RHO, (c) K-SAPO-RHO and (d) Cs-SAPO-RHO at 273 K (black), 298 K (red), 313 K (blue).

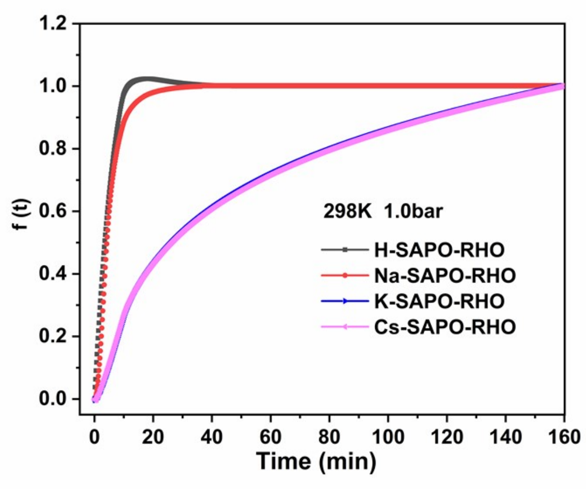

Fig. S5. Rate of adsorption curves for H-SAPO-RHO, Na-SAPO-RHO, K-SAPO-RHO, and Cs-SAPO-RHO of CO_2 at 298K and 1.0bar

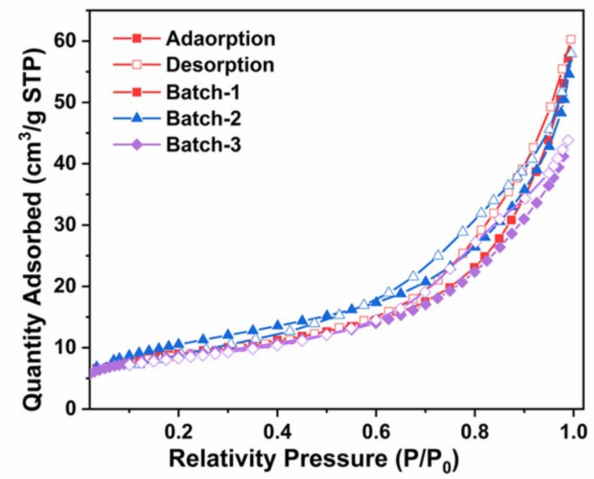

Fig. S6. N_2 adsorption/desorption isotherms of the three batches of Na-SAPO-RHO at 77 K.

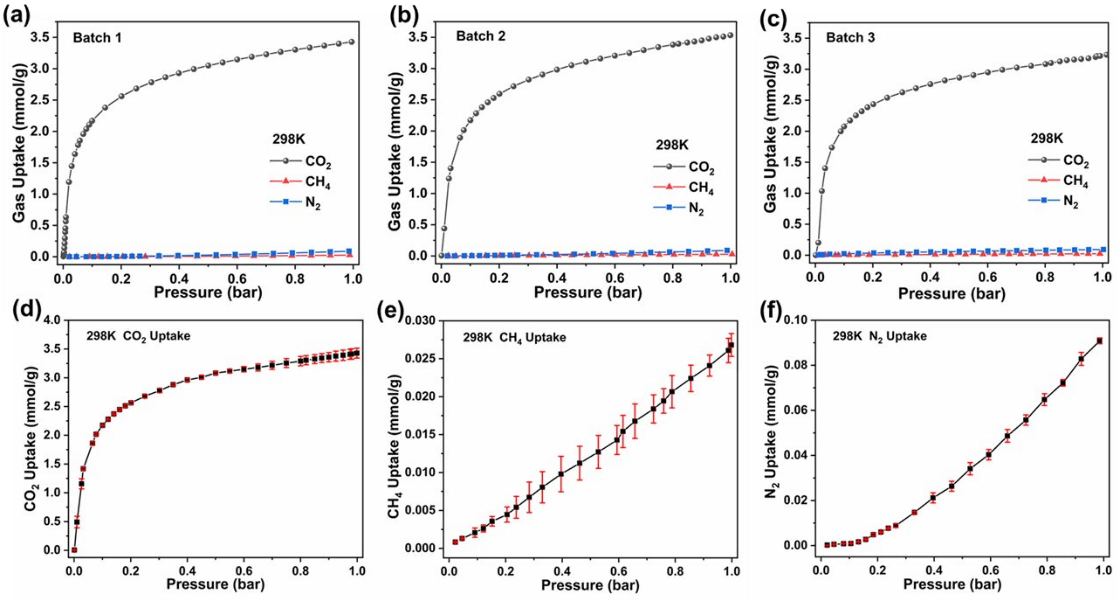

Fig. S7. The pure component adsorption isotherms of the three different batches of Na-SAPO-RHO for CO_2 (a), CH_4 (b), and N_2 (c) and the average uptake of CO_2 (d), CH_4 (e), and N_2 (f) with error bars.

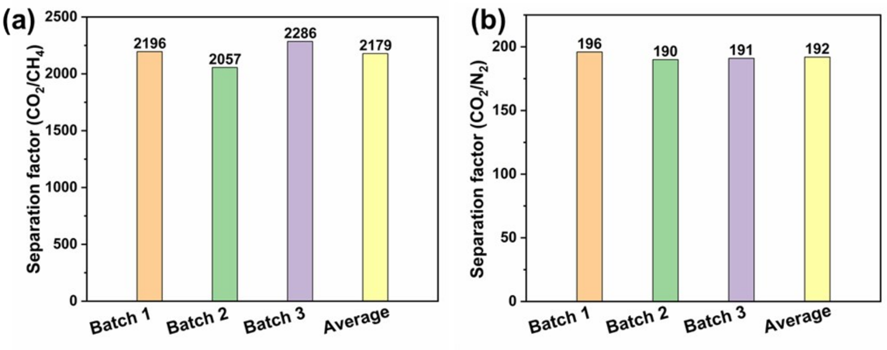

Fig. S8. The separation factors of the three batches of Na-SAPO-RHO for CO_2/CH_4 (a) and CO_2/N_2 (b).

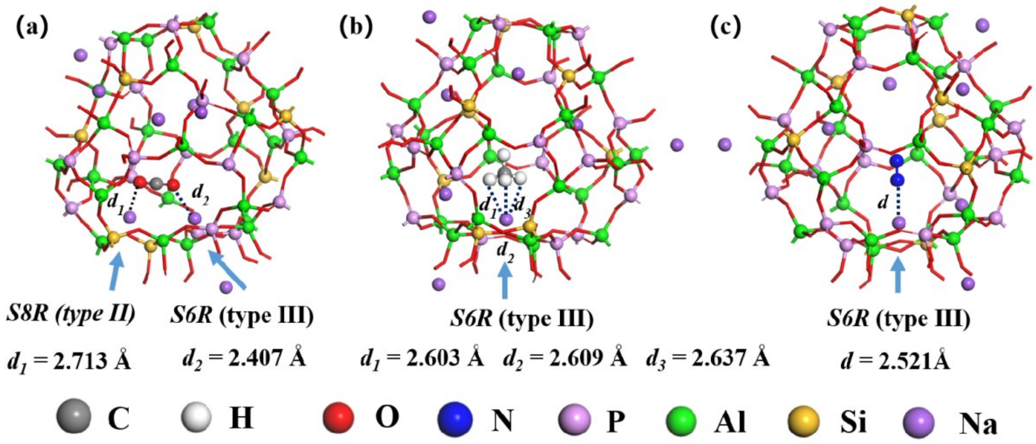

Fig. S9. The optimized adsorption structures of (a) CO_2, (b) CH_4 and (c) N_2 on Na-SAPO-RHO predicted from DFT calculations.

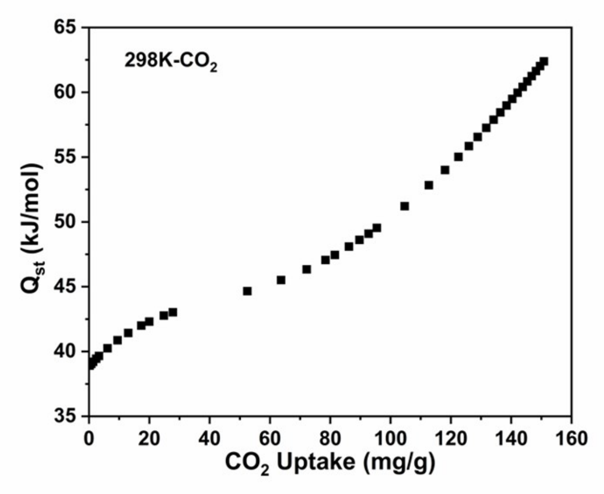

Fig. S10. The isosteric heat of adsorption (Q_{st}) of CO_2 for Na-SAPO-RHO.

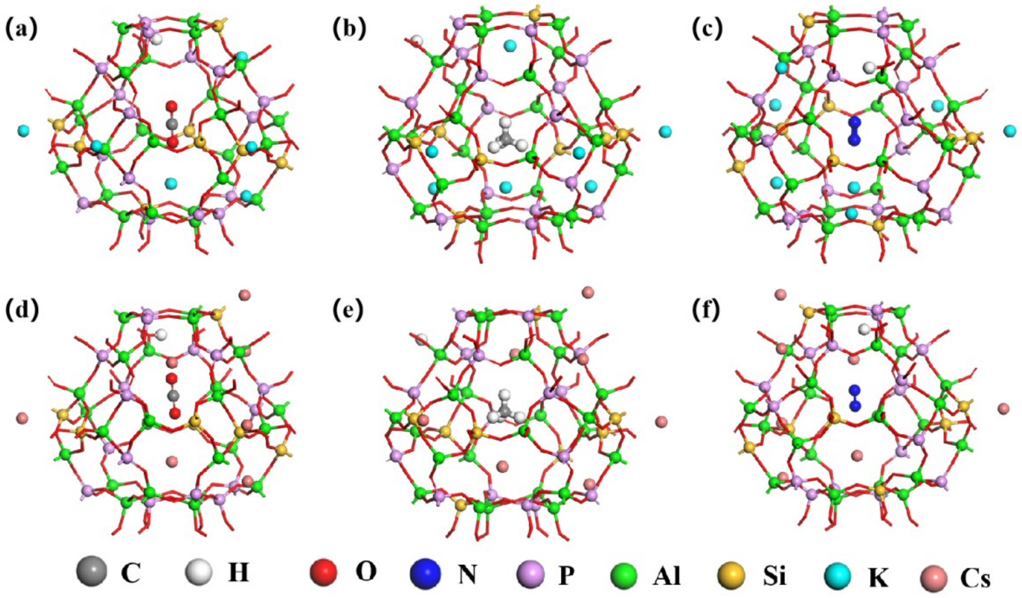

Fig. S11. The optimized adsorption structures of (a) CO_2, (b) CH_4, and (c) N_2 on K-SAPO-RHO and (d) CO_2, (e) CH_4 and (f) N_2 on Cs-SAPO-RHO predicted from DFT calculations.

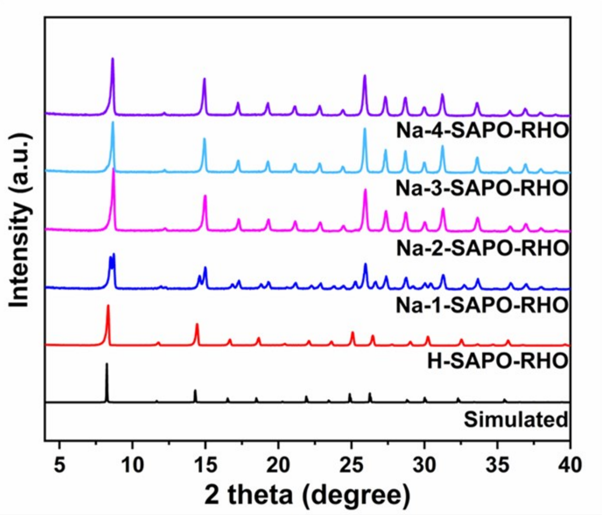

Fig. S12. Simulated PXRD pattern of SAPO-RHO and experimental ones of the calcined Na-SAPO-RHOs.

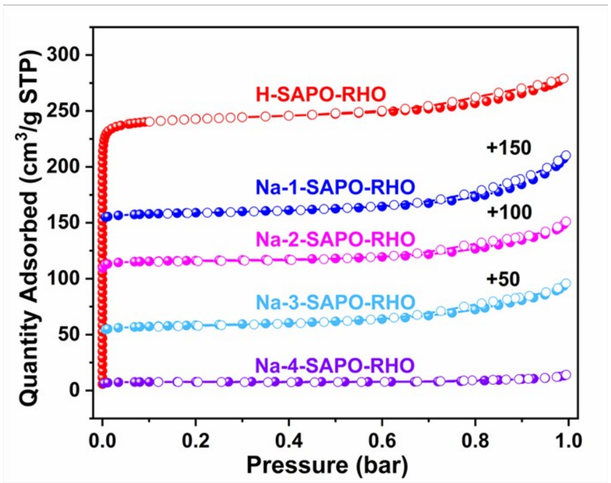

Fig. S13. N_2 adsorption/desorption isotherms of the calcined H-SAPO-RHO and Na-SAPO-RHOs at 77 K.

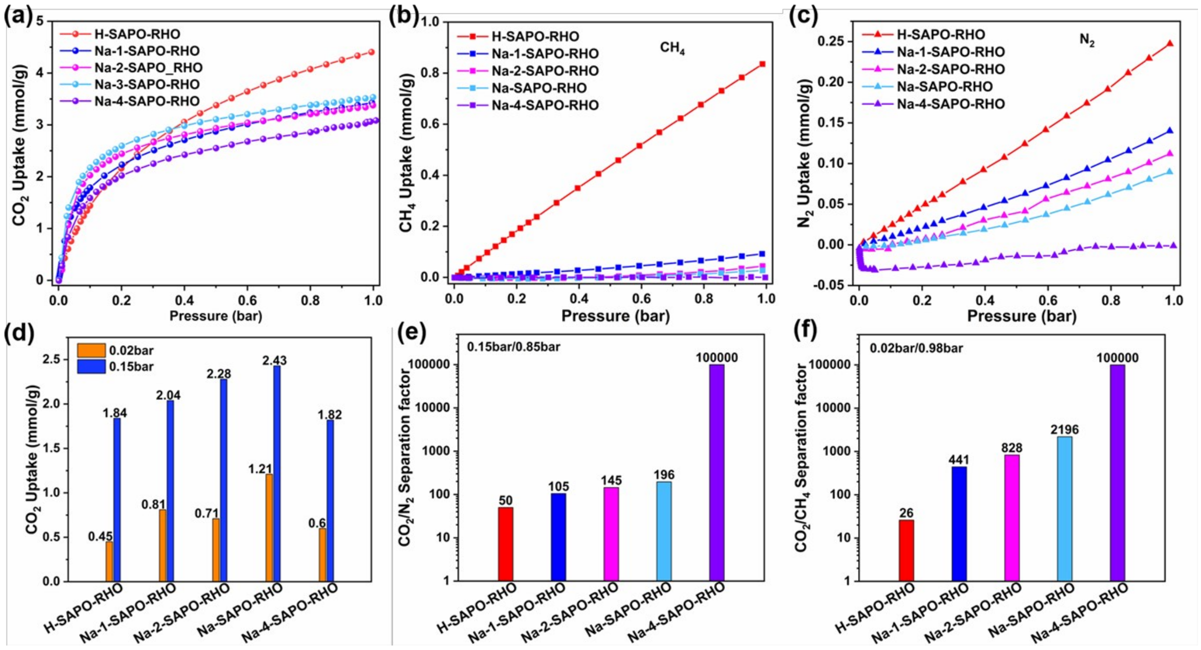

Fig. S14. Comparison of the CO_2 (a), CH_4 (b), and N_2 (c) adsorption isotherms of all Na-SAPO-RHOs at 298 K between 0-1 bar, Comparison of the CO_2 uptake for all Na-SAPO-RHOs under 0.02 and 0.15 bar, respectively at 298 K (d), CO_2/CH_4 separation factors at 0.02/0.98 bar (e), and CO_2/N_2 separation factors at 0.15/0.85 bar (f) at 298 K for all Na-SAPO-RHOs.

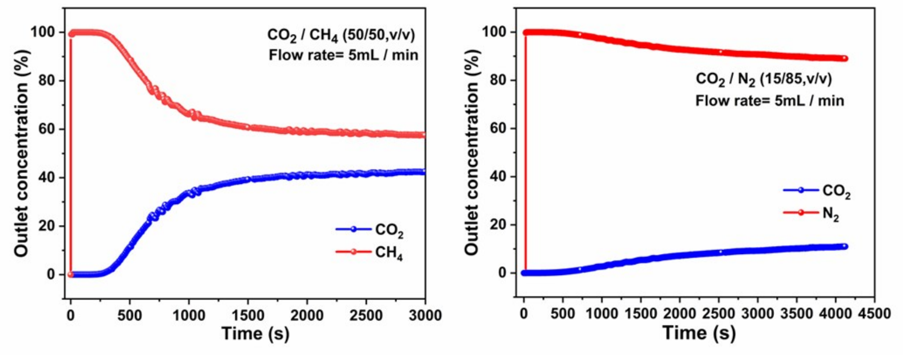

Fig. S15. CO_2/CH_4 (left) and CO_2/N_2 (right) breakthrough curves on Na-SAPO-RHO using CO_2/CH_4 (50:50, v/v) and CO_2/N_2 (15:85, v/v) gas mixtures with a total gas flow rate of 5 mL/min at 298 K, respectively.

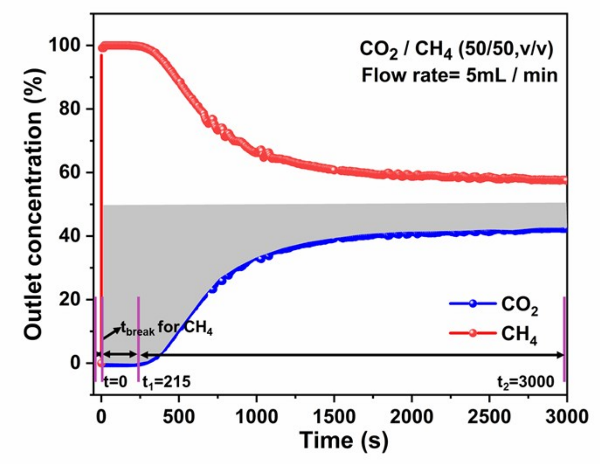

Fig. S16. The breakthrough value estimated from the breakthrough curves for CO_2/CH_4 mixture.

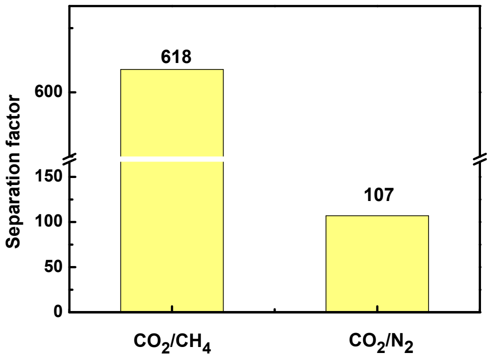

Fig. S17. The dynamic separation factors of the batch 1 of Na-SAPO-RHO for CO_2/CH_4 and CO_2/N_2.

Table S1. The composition and textual properties of H-SAPO-RHO and calcined M-SAPO-RHO (M = Na, K, and Cs).

Sample	Exchange degree (%)	Unit cell compositions of dehydrated sample (EDS)	Surface Area (m^2/g)		Pore Volume (cm^3/g)	
			S_{BET}	S_{micro}	V_{micro}	V_{total}
H-SAPO-RHO	0	$\vert H_{8.7}\vert[Al_{24}Si_{8.7}P_{15.3}O_{96}]$	1001	950	0.350	0.43
Na-SAPO-RHO	87.13	$\vert H_{1.12}Na_{7.58}\vert[Al_{24}Si_{8.7}P_{15.3}O_{96}]$	31	5.5	0.002	0.07
K-SAPO-RHO	65.75	$\vert H_{2.98}K_{5.72}\vert[Al_{24}Si_{8.7}P_{15.3}O_{96}]$	29	4	0.001	0.07
Cs-SAPO-RHO	72.87	$\vert H_{2.36}Cs_{6.34}\vert[Al_{24}Si_{8.7}P_{15.3}O_{96}]$	25	4	0.000	0.06
Na-1-SAPO-RHO	42.41	$\vert H_{3.69}Na_{5.01}\vert[Al_{24}Si_{8.7}P_{15.3}O_{96}]$	54	15	0.020	0.08
Na-2-SAPO-RHO	72.64	$\vert H_{2.38}Na_{6.32}\vert[Al_{24}Si_{8.7}P_{15.3}O_{96}]$	30	5	0.002	0.08
Na-4-SAPO-RHO	100	$\vert Na_{8.70}\vert[Al_{24}Si_{8.7}P_{15.3}O_{96}]$	28	3	0.02	0.07

Table S2. Space groups of aluminosilicate zeolite Rho and SAPO-RHO.

Space group	Aluminosilicate zeolite Rho (**Ref.8**)[7]	SAPO-RHO (this work)
H-type[a]	$Im\bar{3}m$	$I432$ (the sub-group of $Im\bar{3}m$)
Dehydrated cation exchanged	$I\bar{4}3m$	$I23$ (the sub-group of $I\bar{4}3m$)

[a] PXRD data used for structural characterizations were collected in the open environment.

Table S3. Crystallographic details of Rietveld refinements of M-SAPO-RHO samples.

Sample	Na-SAPO-RHO	K-SAPO-RHO	Cs-SAPO-RHO	Cs-SAPO-RHO-hydrated
Space group	$I23$	$I23$	$I23$	$I23$
a(Å)	14.4720(2)	14.46560(10)	14.6832(2)	14.6833(2)
V($Å^3$)	3031.00(7)	3026.98(4)	3165.64(7)	3165.71(7)
R_p	0.01473	0.02768	0.04314	0.03470
R_{wp}	0.02133	0.04324	0.06811	0.04392
R_{exp}	0.01397	0.01283	0.01603	0.02011
R_{bragg}	0.00658	0.01775	0.05352	0.02336
GOF	1.5266	3.3713	4.2486	2.1844
Reflections	440	430	452	463
Parameters	61	60	60	60
Restraints	8	8	8	8
CCDC	2056931	2056929	2056930	2056932

Table S4. Unit cell composition, space group, minimum O-O distance of 8MR windows, minimum M-O distance and cation site occupancies in dehydrated SAPO-RHO (Site I, *d*8*r*; Site II, *s*8*r*; Site III, *s*6*r*) and total M atom in the unit cell.

Sample name	Unit cell composition of dehydrated sample	Unit cell Parameter (Å)	Space group	O···O (Å)	M···O (Å)	Site I (*d*8*r*)		Site II (*s*8*r*)		Site III (*s*6*r*)		Total atom/ Unit cell
						Frac occup	Atom/ unit cell	Frac occup	Atom/ unit cell	Frac occup	Atom/ unit cell	
Na-SAPO-RHO	$\|H_{0.81}Na_{7.89}\|[Al_{24}Si_{8.7}P_{15.3}O_{96}]$	14.4720	*I*23	2.270	2.540	-	-	0.249	5.97	0.240	1.92	7.89
K-SAPO-RHO	$\|H_{2.35}K_{6.35}\|[Al_{24}Si_{8.7}P_{15.3}O_{96}]$	14.4655	*I*23	2.381	2.713	0.228	5.47	-	-	0.110	0.88	6.35
Cs-SAPO-RHO	$\|H_{2.1}Cs_{6.6}\|[Al_{24}Si_{8.7}P_{15.3}O_{96}]$	14.6832	*I*23	2.580	3.185	0.25	6	-	-	0.075	0.6	6.6

Table S5. The textual properties of the three batches of Na-SAPO-RHO.

Sample	Surface Area (m^2/g)		Pore Volume (cm^3/g)	
	S_{BET}	S_{micro}	V_{micro}	V_{total}
Batch 1	31.8	6.0	0.003	0.07
Batch 2	32.5	5.5	0.002	0.07
Batch 3	31.0	5.5	0.002	0.07

Table S6. Calculated adsorption enthalpy H_{ads} (eV) of CO_2, N_2, and CH4 molecule in Na-SAPO-RHO, K-SAPO-RHO, and Cs-SAPO-RHO system.

System	$E_{ads\text{-}SAPO\text{-}RHO}$ **(eV)**	$E_{SAPO\text{-}RHO}$ **(eV)**	E_{ads} **(eV)**	ΔH_{ads}	
				(eV)	**(KJ/mol)**
CO_2-Na-SAPO-RHO	-1152.27		-22.98	-0.44	-42.55
N_2-Na-SAPO-RHO	-1145.74		-16.60	-0.30	-28.61
CH_4-Na-SAPO-RHO	-1153.19		-24.04	-0.31	-30.12
Na-SAPO-RHO		-1128.82			
CO_2-K-SAPO-RHO	-1154.45		-22.98	-0.34	-32.51
N_2-K-SAPO-RHO	-1147.95		-16.60	-0.21	-20.31
CH_4-K-SAPO-RHO	-1155.38		-24.04	-0.21	-20.66
K-SAPO-RHO		-1131.11			
CO_2-Cs-SAPO-RHO	-1153.58		-22.98	-0.31	-29.52
N_2-Cs-SAPO-RHO	-1147.08		-16.60	-0.19	-18.19
CH_4-Cs-SAPO-RHO	-1154.53		-24.04	-0.20	-19.31
Cs-SAPO-RHO		-1130.27			

Table S7. The saturated adsorption amount of CO_2, CH_4, and N_2 of the batch 1 of Na-SAPO-RHO for CO_2/CH_4 and CO_2/N_2.

Binary mixture	CH_4 uptake	CO_2 uptake	N_2 uptake
	cm^3/g	cm^3/g	cm^3/g
CO_2/CH_4 (50/50)	0.0552	34.1	/
CO_2/N_2 (15/85)	/	21.9	1.16

References

1. (a) G. Kresse and J. Hafner, *Phys. Rev. B*, 1993, **47**, 558-561; (b) G. Kresse and J. Furthmüller, *Phys. Rev. B*, 1996, **54**, 11169-11186.
2. J. P. Perdew, K. Burke and M. Ernzerhof, *Phys. Rev. Lett.*, 1996, **77**, 3865-3868.
3. S. Grimme, J. Antony, S. Ehrlich and H. Krieg, *J. Phys. Chem.*, 2010, **132**, 154104.
4. (a) P. E. Blöchl, *Phys. Rev. B*, 1994, **50**, 17953-17979; (b) G. Kresse and D. Joubert, *Phys. Rev. B*, 1999, **59**, 1758-1775.
5. M. J. Frisch, G. W. Trucks, H. B. Schlegel, G. E. Scuseria, M. A. Robb, J. R. Cheeseman, G. Scalmani, V. Barone, G. A. Petersson, H. Nakatsuji, X. Li, M. Caricato, A. V. Marenich, J. Bloino, B. G. Janesko, R. Gomperts, B. Mennucci, H. P. Hratchian, J. V. Ortiz, A. F. Izmaylov, J. L. Sonnenberg, Williams, F. Ding, F. Lipparini, F. Egidi, J. Goings, B. Peng, A. Petrone, T. Henderson, D. Ranasinghe, V. G. Zakrzewski, J. Gao, N. Rega, G. Zheng, W. Liang, M. Hada, M. Ehara, K. Toyota, R. Fukuda, J. Hasegawa, M. Ishida, T. Nakajima, Y. Honda, O. Kitao, H. Nakai, T. Vreven, K. Throssell, J. A. Montgomery Jr., J. E. Peralta, F. Ogliaro, M. J. Bearpark, J. J. Heyd, E. N. Brothers, K. N. Kudin, V. N. Staroverov, T. A. Keith, R. Kobayashi, J. Normand, K. Raghavachari, A. P. Rendell, J. C. Burant, S. S. Iyengar, J. Tomasi, M. Cossi, J. M. Millam, M. Klene, C. Adamo, R. Cammi, J. W. Ochterski, R. L. Martin, K. Morokuma, O. Farkas, J. B. Foresman and D. J. Fox, *Gaussian 16, revision B.01; Gaussian Inc.: Wallingford, CT, 2016.*
6. A. D. Becke, *J. Phys. Chem.*, 1993, **98**, 5648-5652.
7. M. M. Lozinska, E. Mangano, J. P. S. Mowat, A. M. Shepherd, R. F. Howe, S. P. Thompson, J. E. Parker, S. Brandani and P. A. Wright, *J. Am. Chem. Soc.*, 2012, **134**, 17628-17642.